Environmental Science & Technology

pubs.acs.org/est

Article

Unveiling the Position Effect of Ce within Layered MnO_2 to Prolong the Ambient Removal of Indoor HCHO

Chunqi Wang, Jin Chen,* Qiang Li, Shuangyong Su, Hongpeng Jia,* and Hong He*

Cite This: *Environ. Sci. Technol.* 2023, 57, 4598−4607

Read Online

ACCESS | Metrics & More | Article Recommendations | Supporting Information

ABSTRACT: The position of Ce doping has a significant effect on ambient HCHO storage and catalytic oxidation on layered MnO_2. By associating structure and performance, it is unveiled that doping Ce into the in-layered lattice of MnO_2 is favorable to the generation of high-valence Mn cations, enhancing the oxidizing ability and capacity, but an opposite influence is displayed by interlayered Ce doping. From the aspect of energy minimization calculated by DFT, in-layered Ce doping is also recommended due to the decreased energies for molecule adsorption and oxygen vacancy formation. As a result, in-layered Ce-doped MnO_2 displays exceptional activity in catalyzing the deep oxidation of HCHO and a fourfold higher capacity of ambient HCHO storage than pristine MnO_2. The optimal oxide is combined with electromagnetic induction heating to complete the "storage−oxidation" cycle as a promising approach absolutely depending on non-noble oxides and household appliances to realize the long-acting removal of indoor HCHO at room temperature.

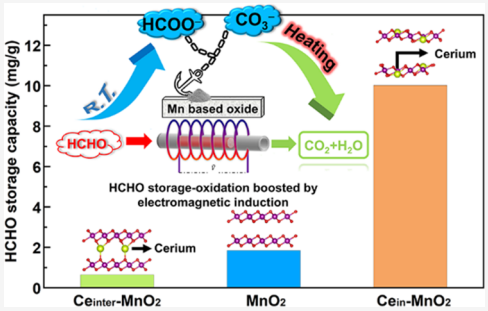

KEYWORDS: *cerium, manganese oxide, electromagnetic induction heating, formaldehyde, storage−oxidation*

1. INTRODUCTION

Air pollution increases the risk of serious cardiovascular and respiratory diseases in human beings, causing approximately 4.9 million deaths worldwide every year.[1] Because of its high toxicity and the long time spent by people in enclosed spaces, formaldehyde (HCHO) is widely considered as the most harmful component among indoor chemical pollutants. Thus, the technological advancement for long-term elimination of indoor HCHO at room temperature has been attracting much attention.[2,3] Because of the low concentration and long release period of indoor HCHO, ambient catalytic oxidation (ACO) is considered as a promising approach. To date, the ACO method mainly depends on supported noble metals including Pt, Pd, and Au.[3−6] For instance, 1% Pt supported on TiO_2 exhibited exceptional performance in catalyzing HCHO oxidation at room temperature, and the promotion effect of alkali metal additives was also found by Zhang et al.[3,7] To reduce the usage of noble metals, the strategy of single-atom dispersion was applied in preparing ACO catalysts.[8−10] However, the ubiquitous and potential application scenarios result in considerable consumption of noble metals beyond their existing reserves.[11−13] Therefore, more attention has recently been paid to developing ACO catalysts without noble metals.

Among various transition metal oxides, the primary activity of manganese oxides (MnO_x) in catalytic oxidation is comparable to that of noble metals due to the abundance of their oxidative species and superior reducibility, according to the literature.[14−16] However, catalytic oxidation of HCHO over MnO_x still requires heating to avoid the gradual decline in its purification ability caused by intermediate accumulation at low temperatures.[17] Fortunately, although the ACO ability of MnO_x tends to decline due to intermediate poisoning, the actual concentration of indoor HCHO is so low (commonly less than 10 ppm) that absolute deactivation takes quite a long time.[18,19] According to the literature, HCHO is oxidized into formic intermediate products ($HCOOH/HCOO^-$) on MnO_x easily at room temperature, but deeper oxidation depends on temperature elevation.[17,18] Because of this, we designed a feasible system of "storage−oxidation" cycle, in which catalysts captured and stored indoor HCHO as intermediates under ambient conditions and then could be regenerated *via* deeply oxidizing the enriched intermediates into CO_2 and H_2O. Considering high safety, easy operation, and wide popularization, an induction stove was used to accomplish catalyst regeneration. Hence, the storage−oxidation cycle was completed by electromagnetic induction heating (EMIH). Considering the longer time taken during storage than during EMIH-driven oxidation, the intermittent model of air purification can even save 99% energy compared with the traditional model of continuous heating, according to a recent

Received: January 16, 2023
Revised: February 23, 2023
Accepted: February 24, 2023
Published: March 7, 2023

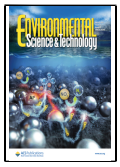

report.[20] To maintain the long-term efficiency of ambient removal of HCHO, catalysts should possess sufficient oxidizing capacity. In a previous study, layered δ-type manganese dioxide (δ-MnO_2) was screened out from various MnO_x, which reduced the HCHO concentration to below the permissible exposure limit of OSHA (0.75 ppm) and could be recycled through simple regeneration using EMIH.[21] To further improve the cycle efficiency, the best approach is to enhance the oxidizing ability to prolong the period of HCHO storage.

Hybridization is widely applied to enhance oxidizing ability.[22−24] Among non-noble additives, cerium (Ce) is always chosen due to its unique capacity for oxygen storage and redox nature.[25,26] For instance, doping Ce with a Ce/Mn ratio = 1/10 was reported to improve the performance of δ-MnO_2 in removing HCHO *via* external heating.[27] Considering the layer-by-layer architecture of δ-MnO_2, Ce cations are possibly located in either the layered matrix or the interlayer space. In fact, the effect of interlayered cations (K^+, Mg^{2+}, Ca^{2+}, and Fe^{3+}) on δ-MnO_2 purifying HCHO was studied by Yu's group.[28] However, the influence of different locations of cationic additives, especially Ce cations, is still unclear. To distinguish the position effect, we attempt to prepare different Ce-doped δ-MnO_2 by means of a one-pot hydrothermal process and hydrothermal ion exchange. By correlating the catalytic performance with characterization and density functional theory (DFT), the underlying principle is unveiled. The decaying period of ambient HCHO storage is greatly prolonged on doping Ce into the layered lattice. As a result, the purification efficiency of the EMIH-enclosed storage−oxidation cycle is improved and keeps steadily.

2. MATERIALS AND METHODS

2.1. Chemicals and Materials. $MnSO_2{\cdot}H_2O$, $Ce(NO_3)_3{\cdot}6H_2O$, $KMnO_4$, 98 wt % H_2SO_4, and paraformaldehyde were purchased from Sinopharm Chemical Reagent Co. Ltd. An aqueous solution containing 5 wt % formaldehyde was prepared *via* hydrothermal depolymerization of paraformaldehyde. In detail, 5 g of paraformaldehyde powder was dispersed in a mixture containing 50 mL of H_2O and 1 mL of H_2SO_4 in a 100 mL Teflon-sealed autoclave, and the solution was heated to 100 °C for 3 h. After cooling to room temperature, the solution was transferred into a flask and then diluted to 100 mL accurately. Further dilution resulted in a 0.125 wt % HCHO solution.

2.2. Preparation of Catalysts. δ-MnO_2 was synthesized by a hydrothermal method according to the literature.[16] $KMnO_4$ (10.50 g) and $MnSO_2{\cdot}H_2O$ (1.93 g) were dissolved with 280 mL of deionized water, sealed in a 400 mL autoclave, then heated to 160 °C, and kept for 48 h. After cooling to room temperature, filtering and calcining at 450 °C in a muffle furnace were carried out for 6 h. Pristine δ-MnO_2 was obtained and named MnO_2.

MnO_2 doped with Ce cations in the in-layer and interlayer were labeled Ce_{in}-MnO_2 and Ce_{inter}-MnO_2, respectively. The synthetic procedures for Ce_{in}-MnO_2 were the same as those for MnO_2, but its formulation was 5.25 g of $KMnO_4$ and 1.78 g of $Ce(NO_3)_3{\cdot}6H_2O$. Ce_{inter}-MnO_2 was prepared *via* ion exchange. In detail, 4 g of MnO_2 was dispersed in 33 mL of $Ce(NO_3)_3$ solution with 1 mol/L concentration for 8 h, then ultrasonically treated for 0.5 h, and separated by centrifugation. The above treatments were repeated twice. Finally, the sediment was washed with deionized water, dried at 100 °C overnight, and calcined at 450 °C for 6 h.

The Ni-supported monolithic catalyst was prepared by flowing the Ce_{in}-MnO_2 slurry through Ni foam in a vacuum coating device, as shown in Figure S1. The Ce_{in}-MnO_2 slurry was obtained by dispersing 100 mg of Ce_{in}-MnO_2 in 5 mL of deionized water. A piece of Ni foam (4×3 cm^2) was filled in a quartz tube (ϕ = 6 mm). Next, the solution was passed through Ni foam under vacuum. This operation was repeated 10 times. After drying at 100 °C overnight, the actual loading amount of Ce_{in}-MnO_2 was 36 mg.

2.3. Characterization. The samples were characterized by scanning electron microscopy (SEM), transmission electron microscopy (TEM), inductively coupled plasma-optical emission spectroscopy (ICP-OES), X-ray diffraction (XRD), N_2 static physisorption, X-ray photoelectron spectroscopy (XPS), H_2 temperature-programmed reduction (H_2-TPR), O_2 temperature-programmed desorption (O_2-TPD), diffuse-reflectance infrared Fourier transform spectroscopy (DRIFTS), and HCHO temperature-programmed oxidation (HCHO-TPO). Detailed procedures for characterization and density functional theory (DFT) calculations are described in the Supporting Information (SI).

2.4. Activity Test. Catalytic oxidation of HCHO was conducted on a fixed bed by filling 66 mg of catalyst pellet (40−60 mesh size) in a quartz tube (ϕ_{in} = 6 mm). The weight hourly space velocity (WHSV) was set at 60,000 mL/(g h). The feed gas (500 ppm HCHO and 3 vol % H_2O) was prepared by passing air through a saturator containing 5 wt % HCHO aqueous solution at room temperature. The passage of feed gas through catalysts was maintained until the HCHO concentration became constant at ambient temperature. Then, the temperature was gradually increased step by step. The concentrations of HCHO and CO_2 were measured by gas chromatography (GC9160). The catalytic performance was assessed on the basis of HCHO conversion and mineralization, i.e., CO_2 formation. The calculation equations are as follows.

$$\text{HCHO conversion}(\%) = \frac{C_{HCHO}^{in} - C_{HCHO}^{out}}{C_{HCHO}^{in}} \times 100\% \tag{1}$$

$$CO_2 \text{ yield } (\%) = \frac{C_{CO_2}^{out}}{C_{CO_2}^{complete}} \times 100\% \tag{2}$$

C_{HCHO}^{in}, C_{HCHO}^{out}, $C_{CO_2}^{out}$, and $C_{CO_2}^{complete}$ correspond to the initial HCHO concentration, outlet HCHO concentration, outlet CO_2 concentration, and CO_2 concentration when HCHO was completely oxidized, respectively.

The storage−oxidation cycle for the removal of indoor HCHO was carried out with feed gas containing 6 ppm HCHO and 3 vol % H_2O in air. The feed gas was obtained by passing an air stream through a 0.125 wt % HCHO aqueous solution at room temperature, and the WHSV was 60,000 mL/(g h). According to breakthrough curves, when the HCHO concentration returned to above 0.5 ppm, the capacity to remove HCHO at the stage of ambient adsorption was assessed. For deep oxidation, the effects of EMIH and furnace heating on catalyst regeneration were tested, respectively. Notably, the temperature of the furnace was controlled at 230 °C, and the EMIH module was powered by 17.4 W. The concentrations of inlet and outlet HCHO were detected by Formaldemeter *htV-M*.

https://doi.org/10.1021/acs.est.3c00420
Environ. Sci. Technol. 2023, 57, 4598−4607

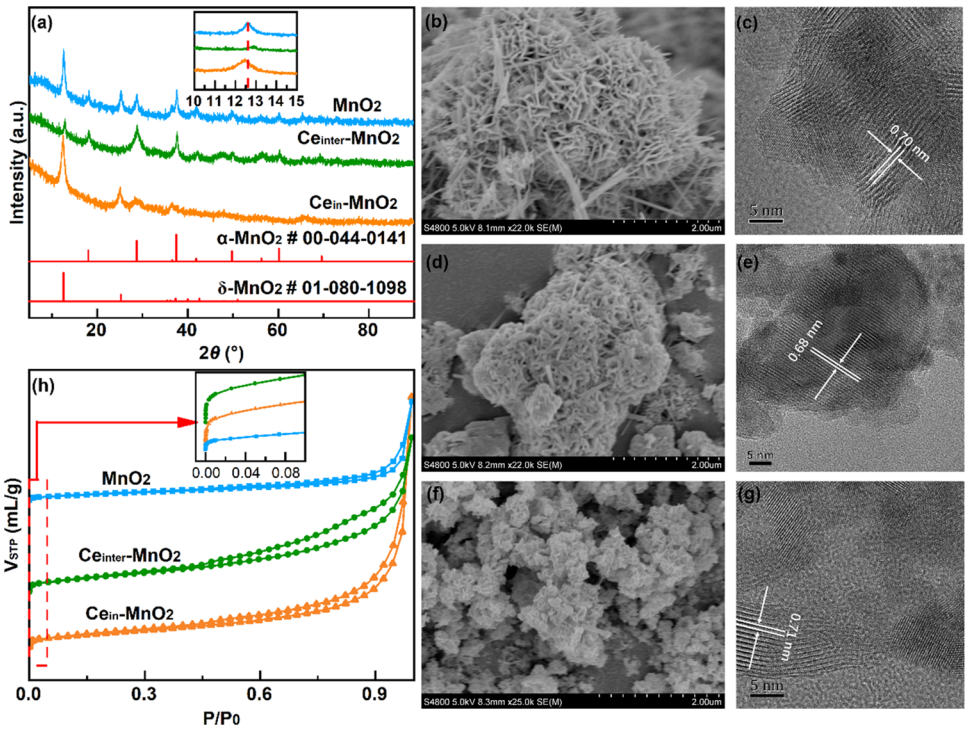

Figure 1. Structural characterization of all samples: (a) XRD patterns. (b, d, f) SEM images of MnO_2, Ce_{inter}-MnO_2, and Ce_{in}-MnO_2, respectively. (c, e, g) TEM images corresponding to MnO_2, Ce_{inter}-MnO_2, and Ce_{in}-MnO_2, respectively. (h) N_2 static adsorption−desorption isotherms.

Table 1. Summary of Characterization and Activity Test Results[a]

sample	interlayer distance (nm)[b]	Ce content (wt %)	K^+ content (wt %)	major pore size (nm)		surface area (m^2/g)		HCHO storage capacity (mg/g)	Ce^{3+}/Ce	AOS[b]
				D_{HK}	D_{BJH}	$S_{Langmuir}$	S_{BET}			
MnO_2	0.70		12.3	0.56	3.90	149.7	35.7	1.84		3.77
Ce_{inter}-MnO_2	0.71	13.9	3.2	0.54	3.70	431.8	88.4	0.64	0.60	3.58
Ce_{in}-MnO_2	0.68	13.7	11.9	0.64	3.90	362.9	75.7	10.02	0.66	3.84

[a]Theoretical interlayer distance was estimated using the Bragg diffraction equation 3, $2d \times \sin\theta = \lambda$, where d is the theoretical interlayer distance, θ is the Bragg angle, and λ is the X-ray wavelength (Cu radiation, 0.154 nm). The average oxidation state (AOS) of Mn was calculated by the binding energy difference (ΔE) of Mn 3s (Figure S10) using the empirical formula AOS = 8.956 − 1.126 × ΔE. [b]Average oxidation state (AOS) of Mn was calculated by the binding energy difference (ΔE) of Mn 3s (Figure S10) using the empirical formula AOS = 8.956 − 1.126 × ΔE.

3. RESULTS AND DISCUSSION

3.1. Textual Properties. As depicted in Figure 1a, because of side reactions during the hydrothermal process, the as-prepared pristine MnO_2 mainly consists of δ-type layered oxide, well indexed to the standard card of 01-080-1098, but is mixed with some α-type tunnel oxide (α-MnO_2 # 00-044-0141). The MnO_2 with interlayer Ce doping (Ce_{inter}-MnO_2) was obtained *via* cation exchange.[29,30] Within Ce_{inter}-MnO_2, characteristic peaks of the α-type tunnel oxide are retained, but those of the δ-type layered oxide become poorer and shift from 12.7 to 13.0°, which implies the presence of Ce cations in the interlayer space causing lattice disorder and shortening the layer distance.[27,31] The one-pot hydrothermal method was used to dope Ce in the in-layer of δ-type MnO_2. The as-prepared Ce_{in}-MnO_2 possesses only the lattice phase of δ-MnO_2 without the α-type oxide, and its sharpest peak is slightly shifted from 12.7 to 12.5° compared with that of pristine MnO_2, indicating the validity of doping Ce into the layer matrix.[32] Based on the peak locations, the interlayer distances in MnO_2, Ce_{inter}-MnO_2, and Ce_{in}-MnO_2 are calculated and displayed in Table 1. As K^+ has a larger ionic radius (0.138 nm) than Ce^{3+} (0.102 nm), the interlayer space would be reduced by replacing K^+ with Ce^{3+}. FTIR spectra (Figure S2) provide more information about the lattice structure. The band at 710 cm^{-1} is assigned to the vibration absorption superposition of the Mn−O−Mn bridging oxygen bond,[33] which appears in pristine MnO_2 and Ce_{inter}-MnO_2. However, the absence of this band in Ce_{in}-MnO_2 indicates that in-layered Ce doping causes crystal and framework modification. With EDS mapping, the element distribution could be visualized. As depicted in Figure S3a−d, pristine MnO_2 consists of Mn, O, and K elements. Meanwhile, Figure S3e−l proves that the Ce element is dispersed homogeneously irrespective of the cation-exchange method or one-pot synthesis. The actual contents of K^+ and introduced Ce^{3+} cations were measured by ICP-OES. As presented in Table 1, the Ce content of Ce_{inter}-MnO_2 is 13.9 wt % and close to that of Ce_{in}-MnO_2 (13.7 wt %). No obvious change occurs to the K^+ content with in-layered Ce doping, but the K^+ content of Ce_{inter}-MnO_2 (3.2 wt %) is remarkably lower than that of MnO_2 (12.3 wt %). Given the role of K^+ in binding layers *via*

https://doi.org/10.1021/acs.est.3c00420
Environ. Sci. Technol. 2023, 57, 4598−4607

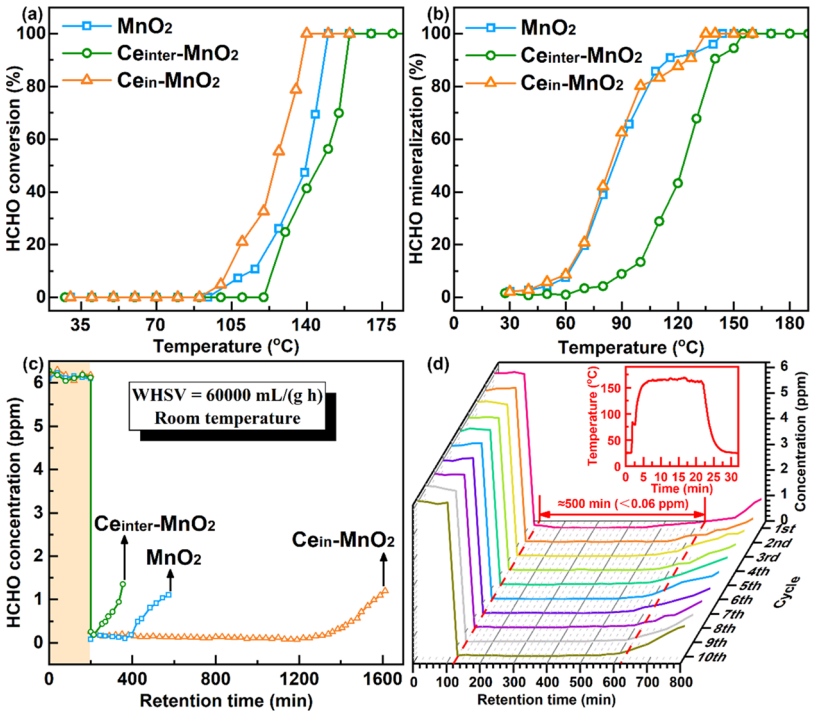

Figure 2. Evaluation of the catalytic performance in removing HCHO. (a, b) Activity profiles from perspectives of conversion and mineralization under conditions of 500 ppm HCHO/humid air, 20% O_2/N_2, and WHSV = 60,000 mL/(g h). (c) Performance in removing 6 ppm HCHO at room temperature. (d) Performance of Ce_{in}-MnO_2 in the intermittent removal of indoor HCHO *via* the EMIH-driven storage−oxidation cycling process.

electrostatic force, the decreasing of its content implies that Ce^{3+} is successfully intercalated into MnO_2 layers.

SEM and TEM were applied to investigate the morphological texture. As shown in Figure 1b, pristine MnO_2 has a flower-like hierarchical architecture composed of δ-MnO_2 sheets and α-MnO_2 rods. Among them, δ-MnO_2 sheets are classic layered oxides with 0.70 nm interplanar spacing along the [001] direction, as shown in Figure 1c.[34] For Ce_{inter}-MnO_2, its oxide sheets downsize, and the layer space decreases to 0.68 nm with interlayered Ce doping, as shown in Figure 1d−e, in accordance with the XRD result. Unlike them, Ce_{in}-MnO_2 consists entirely of small sheets with 0.71 nm interplanar spacing, as depicted in Figure 1f−g. Therefore, the above findings indicate an inevitable relation between Ce doping and the nanostructure.

N_2 static physisorption was carried out to investigate the pore-channel nature. As displayed in Figure 1h, these isotherms belong to the type I curve, of which the sharp adsorption at low pressure ($P/P_0 < 0.1$) indicates the existence of micropores.[35] Size distributions of micropores and mesopores were analyzed with the Horvath−Kawazoe (HK) and Barrett−Joyner−Halenda (BJH) methods, respectively. Analytical results are presented in Figures S4 and S5. Moreover, both the Langmuir and the Brunauer−Emmett−Teller (BET) methods were used to calculate the specific exposed surface area. Calculation results of the major micro-/mesopore sizes and surface areas are summarized in Table 1. Ce_{in}-MnO_2 and Ce_{inter}-MnO_2 have the largest mesopores (3.9 nm). Ce_{in}-MnO_2 has the largest micropores (0.64 nm), which is favorable for mass transfer. Because of the abundance of micropores within MnO_2, the $S_{Langmuir}$ value is much higher than the S_{BET} value. These values are both increased with Ce doping, but the promotion effect is influenced by the different positions of Ce doping. As a result, the S_{BET} value of Ce_{in}-MnO_2 is slightly lower, but its $S_{Langmuir}$ value is much lower than that of Ce_{inter}-MnO_2.

3.2. Performance in Boosting HCHO Oxidation. The performance in catalyzing the oxidation of high-concentration HCHO (500 ppm) was evaluated under conditions of WHSV = 60,000 mL/(g h) and 3 vol % H_2O. The assessment was based on HCHO conversion and mineralization. According to the curve shift of temperature-dependent HCHO conversion, as depicted in Figure 2a, the activities can be ranked in the following order: Ce_{in}-MnO_2 > MnO_2 > Ce_{inter}-MnO_2. Nevertheless, on the basis of HCHO mineralization (Figure 2b), the activity should be rearranged in the following order: Ce_{in}-MnO_2 ≈ MnO_2 > Ce_{inter}-MnO_2. As mentioned before, the largest surface is exposed on Ce_{inter}-MnO_2, but its activity is the poorest in both respects, which means that the surface structure is not crucial to catalytic performance. On comparing the conversion and mineralization curves, we found a seemingly abnormal phenomenon against the law of mass conservation. Particularly, HCHO mineralization is always higher than conversion on each oxide at temperatures between 60 and 130 °C. This phenomenon is related to the formation and transformation of intermediates, according to our previous study.[36] That is, a portion of HCHO is transformed into intermediate products accumulated on catalysts at low temperatures, and then, the deep oxidation of these accumulated intermediates into CO_2 is boosted at elevated temperatures while some incoming HCHO is oxidized deeply. As a result, the overall CO_2 increase is higher than HCHO conversion in a certain temperature range. With the absolute removal of accumulation at high temperatures (over 130 °C), both HCHO conversion and mineralization reach 100% and are subject to carbon balance.

https://doi.org/10.1021/acs.est.3c00420
Environ. Sci. Technol. 2023, 57, 4598−4607

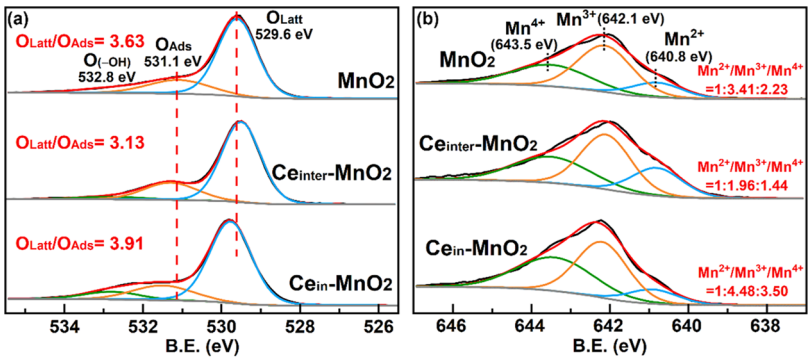

Figure 3. XPS spectra of samples: (a) O 1s and (b) Mn 2p.

According to the behavior of high-concentration HCHO oxidation on various oxides, Mn-based oxides are considered to be potential candidates for ambient abatement of indoor HCHO *via* the storage−oxidation cycle. In this cycle, HCHO is captured by oxides and stored as involatile intermediates at room temperature, and then, the intermediates are oxidized deeply by heating to regenerate catalysts. Because of the low concentration of indoor HCHO normally, the first step of the cycle will last a long time if there are many oxidizing sites, leading to a high capacity of HCHO storage. To examine the storage capacity, the tests were conducted at room temperature using feed gas containing 6 ppm HCHO and 3 vol % H_2O. As depicted in Figure 2c, most of the HCHO is captured by Mn-based oxides, so the concentration decreases sharply from an initial 6 ppm to below 0.1 ppm. However, within a few minutes, the HCHO concentration of the outlet gas from Ce_{inter}-MnO_2 begins to increase. In other words, interlayered Ce-doped MnO_2 exhibits a poorer capacity for ambient HCHO removal than pristine MnO_2. Compared with them, Ce_{in}-MnO_2 requires a much longer time to remove HCHO under the same conditions, and the HCHO concentration in the outlet gas decreases below the indoor limitation of the World Health Organization (0.08 ppm).[37] For convenient comparison, the amount of HCHO captured per unit mass of oxide was calculated. According to the results in Table 1, the capacity of HCHO storage could be ordered as follows: Ce_{in}-MnO_2 > MnO_2 > Ce_{inter}-MnO_2. Compared with pure MnO_2, doping Ce into its in-layered lattice improves the capacity fourfold, obviously, but the capacity declines to about one-third with inter-layered Ce doping, which indicates the position effect of Ce doping.

For easy comparison, recent studies on the application of nonprecious metals in eliminating HCHO are summarized in Table S1. In general, the reaction temperature decreases with the reduction of HCHO concentration and space velocity. Although the reaction conditions are diverse in different reports, causing difficulty in making a precise assessment of activity, the performance of Ce_{in}-MnO_2 in the catalytic oxidation of high-concentration HCHO at high space velocity is moderate on the whole among various oxides (Table S1). Based on the storage−oxidation strategy mentioned above, more importantly, we have greatly improved the storage capacity of Ce_{in}-MnO_2 for the removal of low-concentration HCHO, which is longer than those of δ-MnO_2 (450 min), PC-MnO_x (420 min), and MCO-11 (360 min).[34,36,38] After a period of removing 6 ppm HCHO at room temperature, Ce_{in}-MnO_2 approaches toward failure gradually. Fortunately, the disabled oxide could be reactivated by heating. As depicted in Figure S6, conventional resistance furnace heating to 230 °C could restore the HCHO storage capacity of the disabled Ce_{in}-MnO_2 to the initial level, and the cycle of storage−oxidation process could be repeated steadily three times in the experiment. However, its widespread application is still subject to a limitation, that is, resistance furnaces are commonly seen in laboratories but not popularized in homes due to their low safety and high energy consumption.

As a household heat source, we recommend the utilization of induction stoves, which cook food *via* electromagnetic induction heating (EMIH).[36] In a previous study, MnO_2 powder was loaded on ferromagnetic and conductive Ni foam due to the insensitivity of metal oxides to EMIH. The obtained monolithic material displayed exceptional activity and stability in the ambient removal of HCHO *via* the EMIH-driven storage−oxidation cycle. The experimental process was performed on the electromagnetic equipment we designed (Figure S7a,b). Notably, Ni foam cannot eliminate HCHO, as proven by Figure S8. To examine the validity of in-layered Ce doping to improve the efficiency of the EMIH-driven system, Ce_{in}-MnO_2 was also dispersed on Ni foam (Figure S7c) to test the storage−oxidation cycle. The HCHO concentration is reduced by Ce_{in}-MnO_2/Ni foam from an initial 6 ppm to below 0.06 ppm at ambient temperature, and the endurance time reaches about 500 min, as shown in Figure 2d, which is much longer than that reported for MnO_2/Ni foam (≈200 min) under the same conditions.[36] With the start-up of EMIH powered by 17.4 W, the temperature of the monolithic material increases to around 160 °C rapidly. The increased temperature boosts the regeneration of the deactivated catalyst, so the purification capacity returns to the initial level. During 10 runs of the EMIH-driven storage−oxidation cycle, the high efficiency of HCHO removal is maintained, implying the validity of our designed strategy depending on an induction stove to diminish indoor HCHO at room temperature.

3.4. Physicochemical Properties and Theoretical Calculation. As mentioned above, the position effect of Ce on eliminating HCHO is obviously exhibited, the underlying principle of which is studied by associated physiochemical characterization and density functional theory (DFT). First, the valence state and superficial species were identified by XPS. The Ce^{3+} content was calculated on the basis of the Ce-3d spectrum, as shown in Figure S9. In Table 1, the Ce^{3+}/Ce^{4+} ratio (0.60) of Ce_{inter}-MnO_2 is close to that of Ce_{in}-MnO_2 (0.66), indicating that the variation in structure and performance is primarily due to the position effect rather than the valency difference. As depicted in Figure 3a, the O 1s XPS profile of pure MnO_2 could be fitted into three peaks

https://doi.org/10.1021/acs.est.3c00420
Environ. Sci. Technol. 2023, 57, 4598−4607

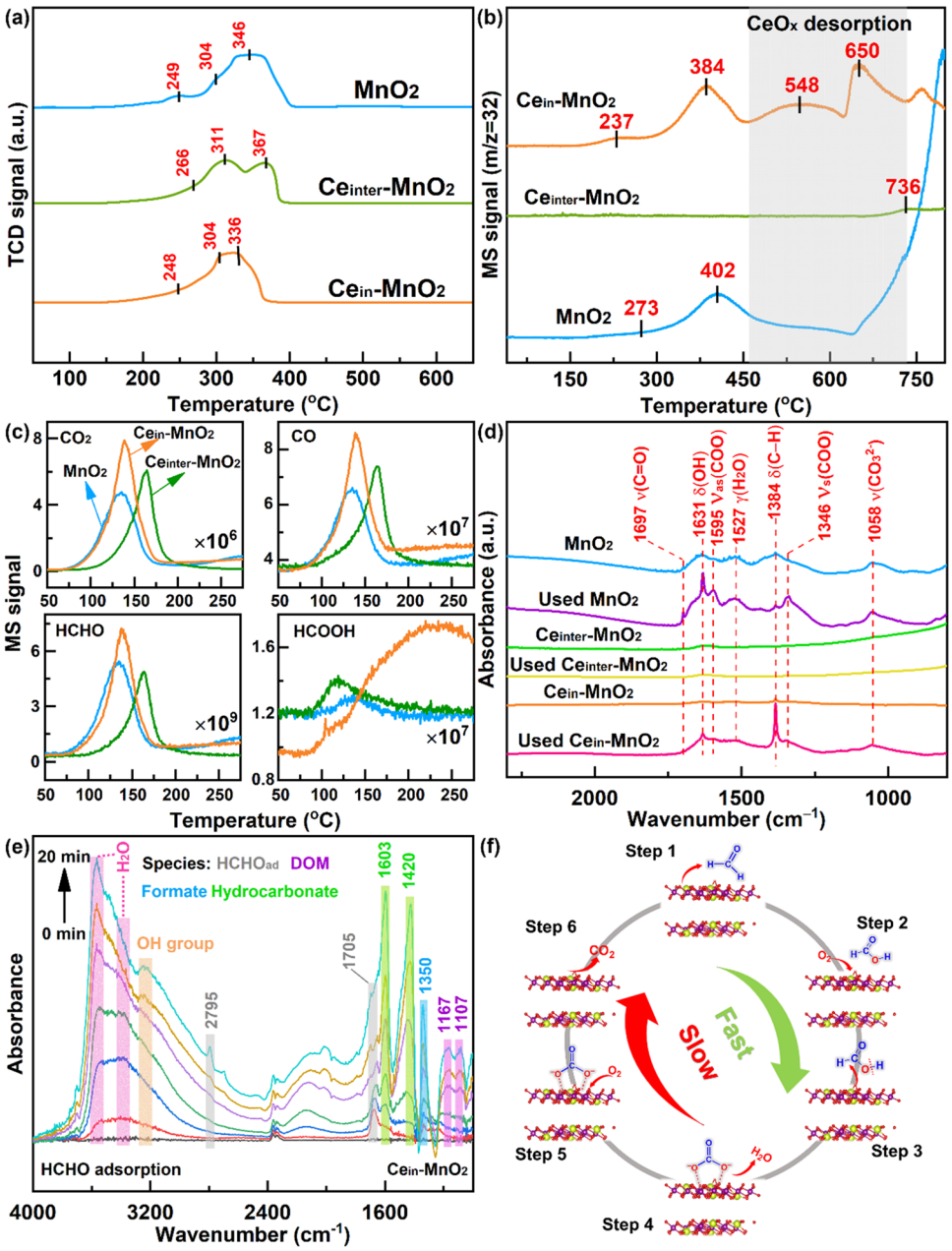

Figure 4. Chemisorption results and DRIFTS characterization. (a) H_2-TPR profiles measured by TCD. (b) O_2-TPD spectra measured by online MS. (c) HCHO-TPO monitored using MS signals of emitted CO_2 (m/z = 44), CO (m/z = 28), HCHO (m/z = 30), and HCOOH (m/z = 46). (d) *Ex situ* DRIFTS results. (e) *In situ* DRIFTS of HCHO adsorption over Ce_{in}-MnO_2 at room temperature. (f) Reaction mechanism of HCHO oxidation over Ce_{in}-MnO_2.

maximized at 532.8, 531.1, and 529.6 eV corresponding to hydroxyl oxygen ($O_{(-OH)}$), adsorbed oxygen (O_{Ads}), and lattice oxygen (O_{Latt}), respectively.[39] According to the peak areas, the O_{Latt}/O_{Ads} ratio of MnO_2 is calculated to be 3.63. With interlayer Ce doping, the O_{Latt} peak shifts to lower binding energies as a result of increased electron density and reduced oxidizing ability of the oxygen species.[40] For many oxidation reactions obeying the Mars−van-Krevelen mechanism, O_{Latt} species displays direct and dominant participation. In fact, the O_{Latt}/O_{Ads} ratio = 3.13 of Ce_{inter}-MnO_2 is lower than that of pristine MnO_2. Obviously, both the weaker oxidizing ability and fewer oxidizing sites are unfavorable to HCHO oxidation on Ce_{inter}-MnO_2. In contrast, in-layered Ce doping results in a positive shift of the O_{latt} peak and a higher O_{Latt}/O_{Ads} ratio (3.91); meanwhile, more $O(_{-OH})$ is preferable for HCHO activation.[15,41] As a result, higher activity and storage capacity are displayed by Ce_{in}-MnO_2.

The above difference in the electronegativity of oxygen species is reflected in the modification of the Mn valence with different positions of Ce doping. As depicted in Figure 3b, the Mn $2p_{3/2}$ profile of pure MnO_2 consists of three peaks at 640.8, 642.1, and 643.5 eV assigned to Mn^{2+}, Mn^{3+}, and Mn^{4+}, respectively.[42] The ratio of different species is 1/3.41/2.23. Interlayered Ce doping facilitates the formation of low-valence Mn^{2+}, so the ratio becomes 1/1.96/1.44. However, in-layered Ce doping increases the content of middle- and high-valence Mn cations, resulting in a ratio of 1/4.48/3.50. Correspondingly, the average oxidation state (AOS) is calculated according

https://doi.org/10.1021/acs.est.3c00420
Environ. Sci. Technol. 2023, 57, 4598−4607

to the Mn 3s-multiplet splitting energy (Figure S10) using an empirical formula (AOS = 8.956 − 1.126 × ΔE) and is displayed in Table 1. The chemical valences of Mn in MnO_2, Ce_{inter}-MnO_2, and Ce_{in}-MnO_2 are calculated to be 3.77, 3.58, and 3.84, respectively, which also follow the above variation of Mn 2p. In general, cations with a higher valence are suitable to withdraw more electrons from oxygen anions due to the stronger electronegativity, which reasonably explains the different oxidizing abilities.[43]

The electronegativity of oxygen species determines the reducibility of metal oxides, which can be characterized by H_2-TPR. With elevated temperature, the reduction passes through $MnO_2 \Rightarrow Mn_2O_3 \Rightarrow Mn_3O_4 \Rightarrow MnO$, leading to three peaks of H_2 consumption by oxygen.[44] In Figure 4a, these peaks appear at 249, 304, and 346 °C for pure MnO_2. Compared with pure oxide, interlayered Ce doping makes these peaks shift to higher temperatures, but doping Ce into the layer promotes the reducibility, causing lower temperatures of H_2 reduction. The position effect of Ce doping also has an influence on the mobility of oxygen species. The O_2-TPD result of pure MnO_2 in Figure 4b shows the desorption of surface-adsorbed oxygen (O_{Surf}) at 273 °C, lattice oxygen on the surface ($O_{Latt,S}$) at 402 °C, and lattice oxygen from the bulk ($O_{Latt,B}$) above 750 °C.[15] The behavior of oxygen desorption becomes complicated with in-layered Ce doping. Compared with pure MnO_2, the peaks of Ce_{in}-MnO_2 at 548 and 650 °C are ascribed to the desorption of CeO_x in a mixed oxide phase.[45] Besides, desorption peaks of MnO_x shift to lower temperatures due to in-layered Ce doping. Because of the prohibition effect of interlayered Ce doping on oxygen mobility, Ce_{inter}-MnO_2 shows only one weak peak at 736 °C. In brief, doping Ce into different positions has an opposite effect on oxygen activity, causing different performances of oxidizing HCHO.

The position effect on oxidizing HCHO was studied by applying HCHO-TPO. During pretreatment, HCHO in a wet stream was captured and stored by oxides at room temperature. At elevated temperatures, various compounds including HCHO, HCOOH, CO, and CO_2 were emitted and identified. In Figure 4c, the signal intensity of the CO_2 fraction is much stronger than those of the others, which indicates that most of the HCHO is completely oxidized over all of the oxides. The CO_2 signal intensity of Ce_{in}-MnO_2 is higher than that of pure MnO_2, indicating its larger storage capacity under the same conditions, which agrees with the activity results. Based on the emission temperature, it is concluded that the complete oxidation of HCHO on Ce_{in}-MnO_2 and pure MnO_2 proceeds more easily than that on interlayered Ce-doped MnO_2. Certainly, some HCOOH and CO as intermediate products could be detected, implying multiple steps of HCHO oxidation over Mn-based catalysts. After the first run of HCHO-TPO, the process of pretreatment and TPO were repeated. Comparing the results of the two runs in Figure S11, no noticeable changes were found to occur in the second run of HCHO-TPO. This indicates that HCHO storage at room temperature causes a reversible modification of structure; thus, the spent oxide can be recovered to the fresh status by heating, which agrees with the performance in the EMIH-driven storage−oxidation cycle. The components in the exhaust gas arising from EMIH-driven regeneration were identified by MS. As shown in Figure S12, vast quantities of CO_2 accompanied by small traces of CO are released under rapid electromagnetic induction heating, which is similar to the HCHO-TPO results, proving the feasibility of the storage−oxidation strategy driven by EMIH.

Ex situ DRIFTS characterization was applied to identify the intermediates produced and accumulated on the oxides at room temperature. Notably, the used samples are the ones that eliminate indoor HCHO at room temperature until penetration. Compared with fresh oxides, several new peaks appear in the spectra of used catalysts, as depicted in Figure 4d. The peaks maximized at 1384, 1595, and 1346 cm^{-1} belong to the C−H bending vibration and asymmetric and symmetric −COO− stretching vibrations, namely, δ(C−H), ν_{as}(COO), and ν_s(COO), of HCOOH/HCOO− species.[46] Meanwhile, the new peak at 1058 cm^{-1} is due to the presence of CO_3^{2-} anions. These results demonstrate that the ACO strategy depends on storing HCHO as formate and carbonate intermediates that are decomposed easily at elevated temperatures, which is in accordance with our previous study.[36]

According to the literature, dioxymethylene (DOM) as a key intermediate always persists at the primary stage of HCHO catalytic oxidation, but in fact, it is not found in the *ex situ* characterization due to its instability, causing rapid transformation into formate.[46] Therefore, *in situ* DRIFTS characterization was further used to investigate the reaction intermediates and mechanisms of HCHO oxidation over Ce_{in}-MnO_2. Figure 4e shows the dynamic changes in the DRIFTS spectra of Ce_{in}-MnO_2 on the basis of the reaction time in a flow of 500 ppm HCHO at room temperature. When Ce_{in}-MnO_2 catalysts were exposed to HCHO, bands were observed at 3580, 3388, 3250, 2795, 1705, 1603, 1420, 1350, 1167, and 1107 cm^{-1}. In detail, the peaks (ν(C−O) = 1167 and 1107 cm^{-1}) belonging to DOM, the peaks ($\nu_{as}(CO_3)$ = 1603 cm^{-1}, $\nu_s(CO_3)$ = 1420 cm^{-1}) attributed to hydrocarbonate species, and the peaks (ν(CH) = 2795 cm^{-1}, ν(C═O) = 1705 cm^{-1}) attributed to HCHO are observed immediately.[2,44,47] Simultaneously, the peaks at 3580 and 3388 cm^{-1} of H_2O and the peak at 3250 cm^{-1} of the −OH group appear.[32] With time, the intensity of the formate peak (δ(CH) = 1350 cm^{-1}) increases, indicating the accumulation of intermediates ($HCOOH/HCOO^-$) on the catalyst. By associating results of *in situ* DRIFTS with physicochemical characterizations, a possible reaction mechanism of HCHO oxidation over Mn-based oxides is shown in Figure 4f (HCHO → CH_2O_2 → $HCOOH/HCOO^-/CO_3^{2-}$ → CO_2 + H_2O). Among the steps, intermediates ($HCOOH/HCOO^-/CO_3^{2-}$) are easily produced by the oxidization of O_{Latt} at room temperature, but their further mineralization into CO_2 has to overcome a higher energy barrier. Therefore, a rather large amount of HCHO is converted into intermediates and accumulated on the catalyst, resulting in the gradual deactivation of non-noble metal catalysts at room temperature.

According to the results of previous characterizations, the position effect of Ce doping influences mainly the modification of the oxidizing ability and capacity. For a deeper insight into the position effect, DFT calculation as a powerful tool of quantitative analysis was used. According to our previous study, an enclosed circle of HCHO catalytic oxidation consists of substrate adsorption, activation, and transformation, while surficial lattice oxygen is consumed, resulting in oxygen vacancies (V_O's). Among them, the crucial processes include adsorption, then conversion of HCHO into DOM, and the donation of lattice oxygen to form V_O. Therefore, the stabilization energy of HCHO and DOM adsorption as well as the V_O formation energy on a typical (001) plane (Abbr.:

https://doi.org/10.1021/acs.est.3c00420
Environ. Sci. Technol. 2023, 57, 4598−4607

E_{Ads}(HCHO), E_{Ads}(DOM), and E_{VO}) were calculated. The calculation results of E_{Ads}(HCHO) in Figure 5a show that

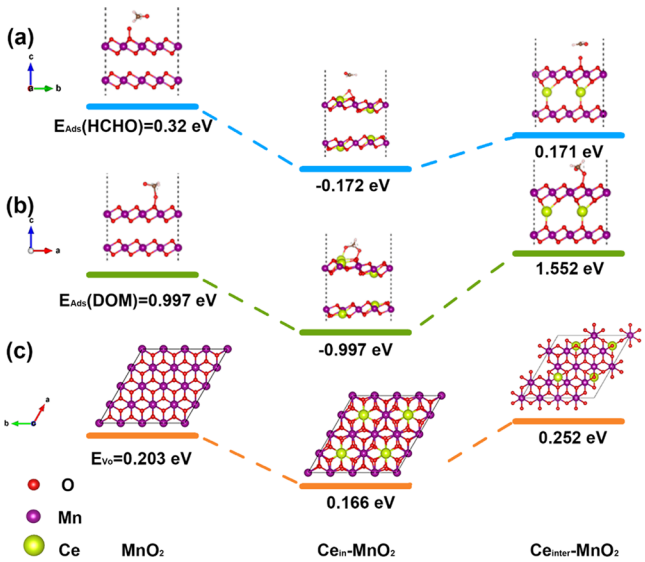

Figure 5. DFT simulation results. (a) Stabilization energy of HCHO adsorption. (b) Stabilization energy of DOM adsorption. (c) Formation energy of oxygen vacancies.

irrespective of Ce doping into the lattice layer or the interlayer space, HCHO adsorption on oxides is enhanced, but a higher promotion effect is exhibited by in-layered doping, resulting in the lowest E_{Ads}(HCHO) (=0.166 eV). DOM adsorption is weakened by interlayer Ce doping, so E_{Ads}(DOM) on Ce_{inter}-MnO_2 (=1.552 eV) is higher than that on pure MnO_2 (=0.997 eV), as shown in Figure 5b. In contrast, in-layered Ce doping facilitates DOM adsorption, which reduces the E_{Ads}(DOM) to −0.997 eV. According to the ascending order of E_{VO} results in Figure 5c, their abilities to donate oxygen to boost the oxidation process could be ranked as follows: Ce_{in}-MnO_2 > MnO_2 > Ce_{inter}-MnO_2. On the basis of all of the above results, although interlayer Ce doping promotes HCHO adsorption, the abilities to stabilize DOM adsorption and generate oxygen vacancy are inhibited, so Ce_{inter}-MnO_2 displays poor activity in removing HCHO compared with pristine MnO_2. However, the three abilities are enhanced simultaneously by doping Ce into layered lattice, thereby leading to a positive position effect on eliminating HCHO.

In summary, the strategy of EMIH-driven storage−oxidation cycles absolutely depends on the utilization of non-noble metal oxides and the widely popularized induction stove to achieve long-acting removal of indoor HCHO at room temperature. While using Ce doping to improve the cleaning efficiency of the cycle system, the position effect of Ce doping on the oxidizing ability and capacity of Mn-based oxide is revealed. The correlation between structure and performance indicates that in-layered Ce doping increases the valence state of Mn cations, causing a higher oxidizing ability and capacity, but interlayer Ce doping has an opposite effect, which is quantitatively illustrated by DFT calculations from the aspects of energy minimization. As a result, in-layered Ce-doped MnO_2 as the optimal oxide has a fourfold higher capacity for HCHO storage than pristine MnO_2 under ambient conditions and could then be reused steadily by EMIH-driven regeneration. The efficient operational mode presented in this study is feasible for the removal of indoor HCHO and improvement of indoor environmental quality.

■ ASSOCIATED CONTENT

Supporting Information

The Supporting Information is available free of charge at https://pubs.acs.org/doi/10.1021/acs.est.3c00420.

Detailed procedures for catalyst characterization, computational details, temperature program characterization (H_2-TPR, O_2-TPD, and HCHO-TPO), vacuum coating device, TEM and EDS mapping, pore size distribution with HK and BJH methods, activity of thermal regeneration, image of the electromagnetic heating device, and cycle experiments of HCHO-TPO (PDF)

■ AUTHOR INFORMATION

Corresponding Authors

Jin Chen − *Xiamen Key Laboratory of Materials for Gaseous Pollutant Control, Institute of Urban Environment, Chinese Academy of Sciences, Xiamen 361021, China; Key Laboratory of Urban Pollutant Conversion, Institute of Urban Environment and CAS Center for Excellence in Regional Atmospheric Environment, Institute of Urban Environment, Chinese Academy of Sciences, Xiamen 361021, China; University of Chinese Academy of Sciences, Beijing 100049, China*; Email: jchen@iue.ac.cn

Hongpeng Jia − *Xiamen Key Laboratory of Materials for Gaseous Pollutant Control, Institute of Urban Environment, Chinese Academy of Sciences, Xiamen 361021, China; Key Laboratory of Urban Pollutant Conversion, Institute of Urban Environment and CAS Center for Excellence in Regional Atmospheric Environment, Institute of Urban Environment, Chinese Academy of Sciences, Xiamen 361021, China; University of Chinese Academy of Sciences, Beijing 100049, China*; orcid.org/0000-0001-9558-5563; Email: hpjia@iue.ac.cn

Hong He − *Key Laboratory of Urban Pollutant Conversion, Institute of Urban Environment and CAS Center for Excellence in Regional Atmospheric Environment, Institute of Urban Environment, Chinese Academy of Sciences, Xiamen 361021, China; University of Chinese Academy of Sciences, Beijing 100049, China; State Key Joint Laboratory of Environment Simulation and Pollution Control, Research Center for Eco-Environmental Sciences, Chinese Academy of Sciences, Beijing 100085, China*; orcid.org/0000-0001-8476-8217; Email: honghe@rcees.ac.cn

Authors

Chunqi Wang − *Xiamen Key Laboratory of Materials for Gaseous Pollutant Control, Institute of Urban Environment, Chinese Academy of Sciences, Xiamen 361021, China; Key Laboratory of Urban Pollutant Conversion, Institute of Urban Environment and CAS Center for Excellence in Regional Atmospheric Environment, Institute of Urban Environment, Chinese Academy of Sciences, Xiamen 361021, China; University of Chinese Academy of Sciences, Beijing 100049, China; College of Resources and Environment, Fujian Agriculture and Forestry University, Fuzhou 350002, China*

Qiang Li − *Xiamen Key Laboratory of Materials for Gaseous Pollutant Control, Institute of Urban Environment, Chinese*

https://doi.org/10.1021/acs.est.3c00420
Environ. Sci. Technol. 2023, 57, 4598−4607

Academy of Sciences, Xiamen 361021, China; Key Laboratory of Urban Pollutant Conversion, Institute of Urban Environment and CAS Center for Excellence in Regional Atmospheric Environment, Institute of Urban Environment, Chinese Academy of Sciences, Xiamen 361021, China; University of Chinese Academy of Sciences, Beijing 100049, China

Shuangyong Su − *Xiamen Key Laboratory of Materials for Gaseous Pollutant Control, Institute of Urban Environment, Chinese Academy of Sciences, Xiamen 361021, China; Key Laboratory of Urban Pollutant Conversion, Institute of Urban Environment and CAS Center for Excellence in Regional Atmospheric Environment, Institute of Urban Environment, Chinese Academy of Sciences, Xiamen 361021, China; University of Chinese Academy of Sciences, Beijing 100049, China; College of Resources and Environment, Fujian Agriculture and Forestry University, Fuzhou 350002, China*

Complete contact information is available at: https://pubs.acs.org/10.1021/acs.est.3c00420

Author Contributions

C.W. performed the experiment, analyzed data, and wrote the paper; J.C. conceived the project, designed the experimental procedure, and participated in writing and revising the article; Q.L. and S.S. took a part in testing the catalytic activity; H.J. and H.H. conceived the project and revised the manuscript. All authors contributed to the development of this article. All authors have approved the final version of the article.

Notes

The authors declare no competing financial interest.

■ ACKNOWLEDGMENTS

This work was funded by the National Nature Science Foundation of China [No. 22176187, 21976172], the CAS Key Laboratory of Urban Pollutant Conversion Joint Research Fund [No. KLUPC-2021-3], the Science and Technology Planning Project of Fujian Province [No. 2020Y0084], the Youth Innovation Promotion Association of CAS [No. 2021304], the FJIRSM&IUE Joint Research Fund [No. RHZX-2019-007], and the National Key Research and Development Program of China [No. 2022YFB3504200].

■ REFERENCES

(1) Zhang, L.; Li, X. Y.; Chen, H. X.; Wu, Z. J.; Hu, M.; Yao, M. S. Haze air pollution health impacts of breath-borne VOCs. *Environ. Sci. Technol.* **2022**, *56*, 8541−8551.

(2) Li, N.; Huang, B.; Dong, X.; Luo, J. S.; Wang, Y.; Wang, H.; Miao, D. Y.; Pan, Y.; Jiao, F.; Xiao, J. P.; Qu, Z. P. Bifunctional zeolites-silver catalyst enabled tandem oxidation of formaldehyde at low temperatures. *Nat. Commun.* **2022**, *13*, No. 2209.

(3) Zhang, C. B.; Liu, F. D.; Zhai, Y. P.; Ariga, H.; Yi, N.; Liu, Y. C.; Asakura, K.; Flytzani-Stephanopoulos, M.; He, H. Alkali-metal-promoted Pt/TiO_2 opens a more efficient pathway to formaldehyde oxidation at ambient temperatures. *Angew. Chem., Int. Ed.* **2012**, *51*, 9628−9632.

(4) Ma, C. Y.; Wang, D. H.; Xue, W. J.; Dou, B. J.; Wang, Hl.; Hao, Z. P. Investigation of formaldehyde oxidation over Co_3O_4-CeO_2 and Au/Co_3O_4-CeO_2 catalysts at room temperature: effective removal and determination of reaction mechanism. *Environ. Sci. Technol.* **2011**, *45*, 3628−3634.

(5) Ye, J. W.; Zhu, B. C.; Cheng, B.; Jiang, C. J.; Wageh, S.; Al-Ghamdi, A. A.; Yu, J. G. Synergy between platinum and gold nanoparticles in oxygen activation for enhanced room-temperature formaldehyde oxidation. *Adv. Funct. Mater.* **2021**, *32*, No. 2110423.

(6) Huang, H. B.; Leung, D. Y. C. Complete oxidation of formaldehyde at room temperature using TiO_2 supported metallic Pd nanoparticles. *ACS Catal.* **2011**, *1*, 348−354.

(7) Zhang, C. B.; He, H.; Tanaka, K.-i. Perfect catalytic oxidation of formaldehyde over a Pt/TiO_2 catalyst at room temperature. *Catal. Commun.* **2005**, *6*, 211−214.

(8) Han, L. L.; Liu, X. J.; Chen, J. P.; Lin, R. Q.; Liu, H. X.; Lu, F.; Bak, S.; Liang, Z. X.; Zhao, S. Z.; Stavitski, E.; Luo, J.; Adzic, R. R.; Xin, H. L. Atomically dispersed molybdenum catalysts for efficient ambient nitrogen fixation. *Angew. Chem. Int. Ed.* **2019**, *58*, 2321−2325.

(9) Kuai, L.; Chen, Z.; Liu, S. J.; Kan, E.; Yu, N.; Ren, Y. M.; Fang, C. H.; Li, X. Y.; Li, Y. D.; Geng, B. Y. Titania supported synergistic palladium single atoms and nanoparticles for room temperature ketone and aldehydes hydrogenation. *Nat. Commun.* **2020**, *11*, No. 48.

(10) Li, Z.; Chen, Y. J.; Ji, S. F.; Tang, Y.; Chen, W. X.; Li, A.; Zhao, J.; Xiong, Y.; Wu, Y.; Gong, Y.; Yao, T.; Liu, W.; Zheng, L.; Dong, J.; Wang, Y.; Zhuang, Z.; Xing, W.; He, C. T.; Peng, C.; Cheong, W. C.; Li, Q.; Zhang, M.; Chen, Z.; Fu, N.; Gao, X.; Zhu, W.; Wan, J.; Zhang, J.; Gu, L.; Wei, S.; Hu, P.; Luo, J.; Li, J.; Chen, C.; Peng, Q.; Duan, X.; Huang, Y.; Chen, X. M.; Wang, D.; Li, Y. Iridium single-atom catalyst on nitrogen-doped carbon for formic acid oxidation synthesized using a general host-guest strategy. *Nat. Chem.* **2020**, *12*, 764−772.

(11) Li, F.; Han, G. F.; Bu, Y. F.; Chen, S. S.; Ahmad, I.; Jeong, H. Y.; Fu, Z. P.; Lu, Y. L.; Baek, J.-B. Unveiling the critical role of active site interaction in single atom catalyst towards hydrogen evolution catalysis. *Nano Energy* **2022**, *93*, 106819.

(12) Shang, Y. N.; Xu, X.; Gao, B. Y.; Wang, S. B.; Duan, X. G. Single-atom catalysis in advanced oxidation processes for environmental remediation. *Chem. Soc. Rev.* **2021**, *50*, 5281−5322.

(13) Sun, R. Y.; Liao, Y. H.; Bai, S. T.; Zheng, M. Y.; Zhou, C.; Zhang, T.; Sels, B. F. Heterogeneous catalysts for CO_2 hydrogenation to formic acid/formate: from nanoscale to single atom. *Energy Environ. Sci.* **2021**, *14*, 1247−1285.

(14) Huang, Y.; Liu, Y.; Wang, W.; Chen, M. J.; Li, H. W.; Lee, S.-c.; Ho, W. K.; Huang, T. T.; Cao, J. J. Oxygen vacancy−engineered δ-MnO_x/activated carbon for room-temperature catalytic oxidation of formaldehyde. *Appl. Catal. B* **2020**, *278*, No. 119294.

(15) Chen, B. B.; Wu, B.; Yu, L. M.; Crocker, M.; Shi, C. Investigation into the catalytic roles of various oxygen species over different crystal phases of MnO_2 for C_6H_6 and HCHO oxidation. *ACS Catal.* **2020**, *10*, 6176−6187.

(16) Zhang, J. H.; Li, Y. B.; Wang, L.; Zhang, C. B.; He, H. Catalytic oxidation of formaldehyde over manganese oxides with different crystal structures. *Catal. Sci. Technol.* **2015**, *5*, 2305−2313.

(17) Zou, N.; Nie, Q.; Zhang, X. R.; Zhang, G. K.; Wang, J. L.; Zhang, P. Y. Electrothermal regeneration by Joule heat effect on carbon cloth based MnO_2 catalyst for long-term formaldehyde removal. *Chem. Eng. J.* **2019**, *357*, 1−10.

(18) Shi, C.; Chen, B. B.; Li, X. S.; Crocker, M.; Wang, Y.; Zhu, A.-m. Catalytic formaldehyde removal by "storage-oxidation" cycling process over supported silver catalysts. *Chem. Eng. J.* **2012**, *200−202*, 729−737.

(19) Zhang, X. M.; Deng, Y. Q.; Tian, P. F.; Shang, H. H.; Xu, J.; Han, Y. F. Dynamic active sites over binary oxide catalysts: In situ/operando spectroscopic study of low-temperature CO oxidation over MnO_x-CeO_2 catalysts. *Appl. Catal. B* **2016**, *191*, 179−191.

(20) Chen, J.; Xu, W. J.; Li, X. L.; Wang, C. Q.; Hu, Z. J.; Jia, H. P. Combining bi-functional Pt/USY and electromagnetic induction for rapid in-situ adsorption-combustion cycling of gaseous organic pollutant. *J. Hazard. Mater.* **2022**, *426*, No. 128097.

(21) Na, C.-J.; Yoo, M.-J.; Tsang, D. C. W.; Kim, H. W.; Kim, K.-H. High-performance materials for effective sorptive removal of formaldehyde in air. *J. Hazard. Mater.* **2019**, *366*, 452−465.

(22) Chen, G.; Rosei, F.; Ma, D. Interfacial reaction-directed synthesis of Ce-Mn binary oxide nanotubes and their applications in

CO oxidation and water treatment. *Adv. Funct. Mater.* **2012**, *22*, 3914−3920.
(23) Huang, J. Z.; Sheng, H. Y.; Ross, R. D.; Han, J. C.; Wang, X. J.; Song, B.; Jin, S. Modifying redox properties and local bonding of Co_3O_4 by CeO_2 enhances oxygen evolution catalysis in acid. *Nat. Commun.* **2021**, *12*, No. 3036.
(24) Huang, Z. F.; Song, J. J.; Du, Y. H.; Xi, S. B.; Dou, S.; Nsanzimana, J. M. V.; Wang, C.; Xu, Z. J.; Wang, X. Chemical and structural origin of lattice oxygen oxidation in Co−Zn oxyhydroxide oxygen evolution electrocatalysts. *Nat. Energy* **2019**, *4*, 329−338.
(25) Trovarelli, A. Catalytic properties of ceria and CeO_2-containing materials. *Catal. Rev.* **1996**, *38*, 439−520.
(26) Murugan, B.; Ramaswamy, A. V.; Srinivas, D.; Gopinath, C. S.; Ramaswamy, V. Nature of manganese species in $Ce_{1-x}Mn_xO_{2-\delta}$ solid solutions synthesized by the solution combustion route. *Chem. Mater.* **2005**, *17*, 3983−3993.
(27) Zhu, L.; Wang, J. L.; Rong, S. P.; Wang, H. Y.; Zhang, P. Y. Cerium modified birnessite-type MnO_2 for gaseous formaldehyde oxidation at low temperature. *Appl. Catal. B* **2017**, *211*, 212−221.
(28) Wang, J. L.; Li, D. D.; Li, P. L.; Zhang, P. Y.; Xu, Q. L.; Yu, J. G. Layered manganese oxides for formaldehyde-oxidation at room temperature: the effect of interlayer cations. *RSC Adv.* **2015**, *5*, 100434−100442.
(29) Gopi, T.; Swetha, G.; Chandra Shekar, S.; Ramakrishna, C.; Saini, B.; Krishna, R.; Rao, P. V. L. Catalytic decomposition of ozone on nanostructured potassium and proton containing δ-MnO_2 catalysts. *Catal. Commun.* **2017**, *92*, 51−55.
(30) Hu, L. Y.; Gao, R.; Zhang, A. Q.; Yang, R.; Zang, X. G.; Wang, S. Y.; Yao, S. Y.; Yang, Z. Y.; Hao, H. G.; Yan, Y. M. Cu^{2+} intercalation activates bulk redox reactions of MnO_2 for enhancing capacitive performance. *Nano Energy* **2020**, *74*, No. 104891.
(31) Dong, C.; Qu, Z. P.; Jiang, X.; Ren, Y. W. Tuning oxygen vacancy concentration of MnO_2 through metal doping for improved toluene oxidation. *J. Hazard. Mater.* **2020**, *391*, No. 122181.
(32) Chen, J.; Jiang, M. Z.; Xu, W. J.; Chen, J.; Hong, Z. X.; Jia, H. P. Incorporating Mn cation as anchor to atomically disperse Pt on TiO_2 for low-temperature removal of formaldehyde. *Appl. Catal. B* **2019**, *259*, No. 118013.
(33) Dong, N.; Chen, M. Y.; Ye, Q.; Zhang, D.; Dai, H. X. Promotional effect of cobalt doping on catalytic performance of cryptomelane-type manganese oxide in toluene oxidation. *J. Environ. Sci.* **2023**, *126*, 263−274.
(34) Wang, M.; Zhang, L. X.; Huang, W. M.; Xiu, T. P.; Zhuang, C. G.; Shi, J. L. The catalytic oxidation removal of low-concentration HCHO at high space velocity by partially crystallized mesoporous MnO_x. *Chem. Eng. J.* **2017**, *320*, 667−676.
(35) Thommes, M.; Kaneko, K.; Neimark, A. V.; Olivier, J. P.; Rodriguez-Reinoso, F.; Rouquerol, J.; Sing, K. S. W. Physisorption of gases, with special reference to the evaluation of surface area and pore size distribution (IUPAC Technical Report). *Pure Appl. Chem.* **2015**, *87*, 1051−1069.
(36) Wang, C. Q.; Chen, J.; Xu, W. J.; Li, X. L.; Jia, H. P. Cooking-like regeneration prolonging the catalytic lifetime for ambient removal of indoor HCHO. *ACS ES&T Eng.* **2022**, *2*, 1229−1238.
(37) Ye, J. W.; Yu, Y.; Fan, J. J.; Cheng, B.; Yu, J. G.; Ho, W. Room-temperature formaldehyde catalytic decomposition. *Environ. Sci. Nano* **2020**, *7*, 3655−3709.
(38) Li, H. W.; Ho, W. K.; Cao, J. J.; Park, D.; Lee, S.-c.; Huang, Y. Active complexes on engineered crystal facets of MnO_x-CeO_2 and scale-up demonstration on an air cleaner for indoor formaldehyde removal. *Environ. Sci. Technol.* **2019**, *53*, 10906−10916.
(39) Li, H. F.; Lu, G. Z.; Dai, Q. G.; Wang, Y. Q.; Guo, Y.; Guo, Y. L. Efficient low-temperature catalytic combustion of trichloroethylene over flower-like mesoporous Mn-doped CeO_2 microspheres. *Appl. Catal. B* **2011**, *102*, 475−483.
(40) Li, Y. B.; Zhang, C. B.; He, H.; Zhang, J. H.; Chen, M. Influence of alkali metals on Pd/TiO_2 catalysts for catalytic oxidation of formaldehyde at room temperature. *Catal. Sci. Technol.* **2016**, *6*, 2289−2295.
(41) Wang, J. L.; Zhang, P. Y.; Li, J. G.; Jiang, C. J.; Yunus, R.; Kim, J. Room-temperature oxidation of formaldehyde by layered manganese oxide: effect of water. *Environ. Sci. Technol.* **2015**, *49*, 12372−12379.
(42) Chen, J.; Yan, D. X.; Xu, Z.; Chen, X.; Chen, X.; Xu, W. J.; Jia, H. P.; Chen, J. A novel redox precipitation to synthesize Au-doped alpha-MnO_2 with high dispersion toward low-temperature oxidation of formaldehyde. *Environ. Sci. Technol.* **2018**, *52*, 4728−4737.
(43) Dai, Z. J.; Zhu, J.; Yan, J. Q.; Su, J. F.; Gao, Y. F.; Zhang, X.; Ke, Q. F.; Parsons, G. N. An advanced dual-function MnO_2-fabric air filter combining catalytic oxidation of formaldehyde and high-efficiency fine particulate matter removal. *Adv. Funct. Mater.* **2020**, *30*, No. 2001488.
(44) Wang, Y.; Liu, K.; Wu, J.; Hu, Z. M.; Huang, L.; Zhou, J.; Ishihara, T.; Guo, L. M. Unveiling the effects of alkali metal ions intercalated in layered MnO_2 for formaldehyde catalytic oxidation. *ACS Catal.* **2020**, *10*, 10021−10031.
(45) Chen, J.; Wang, C. Q.; Lv, X. L.; Huang, G. X.; Xu, W. J.; Li, X. L.; Jia, H. P. Pt/CeO_2 coated with polyoxometallate chainmail to regulate oxidation of chlorobenzene without hazardous by-products. *J. Hazard. Mater.* **2023**, *441*, No. 129925.
(46) Wang, J. L.; Li, J.; Zhang, P. Y.; Zhang, G. K. Understanding the "seesaw effect" of interlayered K^+ with different structure in manganese oxides for the enhanced formaldehyde oxidation. *Appl. Catal. B* **2018**, *224*, 863−870.
(47) Yusuf, A.; Sun, Y.; Liu, S.; Wang, C.; Ren, Y.; Xiao, H.; Snape, C.; He, J. Study of the effect of ceria on the activity and selectivity of Co and Ce co-doped birnessite manganese oxide for formaldehyde oxidation. *J. Hazard. Mater.* **2022**, *424*, No. 127583.

https://doi.org/10.1021/acs.est.3c00420
Environ. Sci. Technol. 2023, 57, 4598−4607